

Low Dose CT for Stroke Diagnosis: A Dual Pipeline Deep Learning Framework for Portable Neuroimaging

Rhea Ghosal^{a,*}, Ronok Ghosal^b, Eileen Lou^c

^a*Westlake High School, Austin, TX, USA*

^b*California Institute of Technology, Pasadena, CA, USA*

^c*Round Rock High School, Round Rock, TX, USA*

Abstract

Portable CT scanners offer a promising path to early stroke detection in ambulatory and pre-hospital low-resource environments, but reduced radiation doses introduce substantial noise that degrades image quality and diagnostic reliability. We present a deep learning framework for stroke classification from simulated low-dose CT (LDCT) brain scans, aimed at enabling reliable AI-assisted triage in mobile clinical settings. Controlled levels of Poisson noise were applied to high-dose CT images to replicate statistical noise patterns in portable scanners. Our system includes two pipelines: (1) direct classification of noisy LDCT images using a convolutional neural network, and (2) sequential denoising followed by classification. We evaluated model performance across multiple dose levels using accuracy, sensitivity, and AUC. While the denoise+classify pipeline improved how the images looked, it did not reliably improve classification. In several settings, direct classification on noisy scans was more sensitive for stroke detection. This trade-off between image quality and diagnostic reliability suggests that benchmark results should be reported for both approaches. It also raises the possibility that future systems may need hybrid models that learn denoising and classification together. Our best denoise-then-classify pipeline achieved 0.94 AUC and 0.91 accuracy at 10% dose, outperforming direct classification by 6%. Unlike prior LDCT studies that focus on either denoising or clean-image classification, our work benchmarks stroke classification performance across multiple simulated dose levels and artifact conditions. By comparing direct classification and denoise-then-classify pipelines, we reveal a trade-off between perceptual quality and diagnostic sensitivity, establishing a practical, reproducible baseline for portable CT-based stroke triage. Our analysis covers hemorrhagic stroke only (RSNA ICH dataset). These results demonstrate the potential for AI-assisted LDCT analysis to support rapid stroke triage in pre-hospital and mobile care environments. We do not assess ischemic stroke here, so findings should be read in that context. Validating on ischemic cohorts, multi-center data, and real portable CT devices is an important next step.

*Corresponding author

Email address: grhea1008@gmail.com (Rhea Ghosal)

Keywords

Stroke triage, low-dose CT (LDCT), portable CT, deep learning, denoising, U-Net, ResNet, dose-aware evaluation, motion/ring artifact stress tests, portable neuroimaging.

Introduction

The emergence of portable CT scanners offers a compelling alternative for decentralized, point-of-care and prehospital neuroimaging. Yet, these systems must operate at reduced radiation doses to ensure patient safety and device miniaturization. Low-dose CT (LDCT) suffers from photon starvation and Poisson noise, degrading image quality and impairing both clinical interpretation and downstream AI tools.

We build and evaluate a dual-pipeline deep learning framework for efficient stroke classification under LDCT constraints. We simulate dose-reduced scans by applying Poisson noise, reflecting photon statistics in X-ray acquisition, to high-quality brain CT images, mimicking the physical characteristics of low-dose acquisition. Our approach compares two pipelines: one that directly classifies noisy LDCT images using a convolutional neural network, and another that first applies deep denoising via a U-Net architecture before classification. We assess both pipelines at different simulated dose levels ($\lambda \in 1, 2, 5, 10, 20, 40$) and evaluate robustness under artifact stress tests (motion and ring). At high noise, denoising restored image quality (e.g., PSNR up to 4.978 dB at $\lambda = 5, 20$). However, diagnostic reliability was inconsistent, revealing a trade-off between perceptual quality and utility.

This work provides a systematic baseline for LDCT stroke triage using simulated doses and artifact stress tests. It supports the development of portable, low-power, real-time stroke assessment systems deployable in ambulances, remote clinics, and field operations.

Related Work

Deep learning has become central to CT imaging, particularly in denoising and pathology detection. Earlier hand-crafted methods such as BM3D [1] and Non-Local Means reduce noise but tend to blur subtle anatomical features at low signal-to-noise ratios (SNR).

Models like DnCNN [2], RED-Net [3], and U-Net [4] learn direct mappings from noisy to clean images and report strong Peak Signal-to-Noise Ratio (PSNR) and Structural Similarity Index Measure (SSIM) scores [5]. However, these networks require large datasets and remain difficult to deploy on lightweight or hardware-constrained hardware.

Convolutional neural networks such as ResNet [6] and DenseNet [7] have also been applied to stroke classification from CT and MRI. Most of these studies

assume clean, high-quality scans and do not address the noise introduced by low-dose portable imaging or evaluate diagnostic endpoints under dose reduction.

Few studies benchmark classification accuracy across simulated dose levels or quantify robustness under acquisition artifacts (e.g., motion, ring) or directly compare denoising and classification pipelines in portable neuroimaging. Here, we evaluate both pipelines under noisy, low-dose conditions. Portable CT scanners are already being used in stroke care, including in ambulance-based stroke units [8, 9], making this evaluation clinically relevant.

Transformer-based models such as SwinIR [10], Restormer [11], and TransUNet [12] extend CNN-based methods by modeling long-range dependencies with self-attention. They achieve state-of-the-art results in image restoration and biomedical imaging, and their success suggests future opportunities for LDCT classification and for end-to-end objectives that jointly optimize denoising and diagnosis under low-dose and artifact shifts.

Methods

Dataset and Preprocessing

We used the RSNA Intracranial Hemorrhage Detection dataset from Kaggle [13], a public, de-identified collection, which contains tens of thousands of labeled CT slices across multiple hemorrhage subtypes. The DICOM files were converted to PNG format and normalized to grayscale values in the range [0, 1].

Although the dataset was designed for hemorrhage detection rather than full stroke triage, it is well suited to our study. Hemorrhagic stroke is a major subtype where early recognition is critical, and the images capture contrast differences between parenchyma, hematoma, and background that are particularly sensitive to noise in low-dose CT. Since ischemic cases are not included, our analysis is limited to hemorrhagic stroke. Future extensions could incorporate ischemic cohorts, multi-center data, or structured synthetic augmentation to broaden applicability and external validity.

The data consisted of axial slices resized to 128×128 with binary labels marking whether hemorrhage was present. The dataset was already partitioned into train/validation/test folders at the patient level. We preserved these fixed splits for all experiments, ensuring patient-level separation with no cross-patient leakage. These fixed splits were reused across all experiments, ensuring that multi-run statistics reflect only model-level randomness (e.g., weight initialization and data augmentation) rather than changes in the evaluation set. To improve generalization, the training set was augmented with random rotations, flips, and translations. Since the RSNA scans were high-dose, we simulated low-dose conditions by adding controlled, physically motivated Poisson noise, which reproduces realistic LDCT photon statistics while retaining the benefits of a large, validated dataset. Augmentation was applied only during training to prevent leakage into validation or test data, and all stochastic procedures (e.g., augmentation, weight initialization) used fixed random seeds for reproducibility.

Robustness Evaluation Protocol

Models are evaluated under three settings: (i) clean HDCT, (ii) simulated LDCT doses ($\lambda \in \{1, 5, 10, 20, 40\}$), and (iii) acquisition artifacts (motion, ring) across severities $s \in \{1, \dots, 5\}$. Metrics include Accuracy, ROC-AUC, Sensitivity, and F1; all discrete metrics are computed at a probability threshold of 0.5 on a held-out test set. We also assess calibration via Expected Calibration Error (ECE; 15 equal-width probability bins). We report per-dose PSNR/SSIM and per-severity robustness deltas (ΔAUC , ΔAcc) to separate perceptual gains from diagnostic utility. Additionally, we report per-image metrics and aggregate patient-level summaries to ensure clinical interpretability. Finally, we measure inference latency on a single NVIDIA RTX 3070 (8 GB VRAM) and on CPU-only to gauge deployability in resource-constrained settings. We verified that the severity schedule was applied identically to both pipelines.

Low Dose Simulation

To simulate realistic low-dose CT (LDCT) data, we applied Poisson noise to each high-dose CT (HDCT) image $I(x, y)$ according to:

$$I_{\text{LD}}(x, y) \sim \frac{1}{\lambda} \text{Poisson}(\lambda I(x, y))$$

where $I(x, y) \in [0, 1]$ denotes the normalized HDCT intensity and λ is the dose scaling factor (smaller $\lambda \Rightarrow$ lower dose, higher noise).

Here, λ is the dose scaling factor; smaller values of λ correspond to lower simulated radiation doses and thus noisier images. We experimented with multiple dose levels: $\lambda \in \{1, 5, 10, 20, 40\}$. In our pipeline, these LDCT images were generated on-the-fly during training and evaluation using a controlled noise simulation function, with outputs clipped to $[0, 1]$ to maintain valid intensity ranges and fixed random seeds for reproducibility. Low-dose CT imaging has been widely studied in other contexts such as lung cancer screening, where controlled dose-reduction benchmarks have established realistic simulation protocols [14].

Portable-CT Artifact Simulation (Motion & Ring)

Beyond photon-limited Poisson noise, portable CT acquisitions frequently exhibit motion and ring artifacts due to patient movement and detector non-idealities. To approximate these effects, we introduce two parameterized corruptions applied on top of the LDCT image I_{LD} .

Motion blur. We model in-plane motion as a linear motion kernel k_{mot} of length L and angle θ , convolving the image:

$$I_{\text{mot}} = I_{\text{LD}} * k_{\text{mot}}(L, \theta), \quad L \in \{3, 5, 7\}, \quad \theta \sim \mathcal{U}(0^\circ, 180^\circ).$$

This captures short translational motion typical in rapid, portable scans and is applied with antialiasing-safe padding to avoid boundary artifacts.

Ring artifacts. Detector gain drifts can yield concentric rings in reconstructed slices. We synthesize rings by superimposing radially varying bands:

$$I_{\text{ring}}(r, \phi) = I_{\text{base}}(r, \phi) (1 + \alpha \cdot s(r)),$$

where $I_{\text{base}} \in \{I_{\text{LD}}, I_{\text{mot}}\}$, r is radius from the slice center, $s(r)$ is a sparse sum of narrow Gaussian bands at random radii, and $\alpha \in \{0.02, 0.05, 0.10\}$ controls artifact strength (bands are randomly placed but fixed per image once sampled).

Severity scale. For stress testing, we define corruption severities $s \in \{1, \dots, 5\}$ by jointly increasing $(\lambda^{-1}, L, \alpha)$.¹ This yields realistic stress scenarios for portable CT beyond pure Poisson noise, with the same severity schedule applied to both pipelines to enable fair, paired comparisons.

Model Architectures

As shown in Figure 1, we designed two pipelines for comparison: **Pipeline 1 (Direct Classification)**: A ResNet-18 convolutional neural network takes noisy single-channel LDCT images as input and outputs stroke/no-stroke probabilities. ResNet-18 was selected as the classifier because it provides a good trade-off between performance and runtime. This helps lightweight or portable systems. **Pipeline 2 (Denoising + Classification)**: Before classification, we add a denoising step. The denoiser is a U-Net, an encoder-decoder network with skip connections that was first introduced for medical image tasks. It was chosen because it can clean noise while still keeping structural details needed for diagnosis. The U-Net and classifier are trained sequentially (U-Net on reconstruction; ResNet-18 on denoised outputs), and the classifier uses the same architecture as Pipeline 1 but is trained independently (no weight sharing). The denoised slices were then classified with the same ResNet-18 used in Pipeline 1. Both models were implemented in PyTorch with standard He initialization and batch normalization, and inputs were resized to 128×128 grayscale as described above. Figure 1 illustrates the two-pipeline design.

Reproducibility.

All experiments were implemented in Python (PyTorch for deep models; scikit-learn for logistic regression). BM3D denoising used the public `bm3d` package with inputs normalized to $[0, 1]$; code to reproduce the BM3D+LR pilot is provided in our repository and uses the identical test split and random seed protocol.

Experiments

Experimental Setup

We trained and evaluated both pipelines using the preprocessed LDCT dataset with five dose levels: $\lambda \in \{1, 5, 10, 20, 40\}$. For each dose, we created

¹E.g., higher s lowers λ and increases L and α .

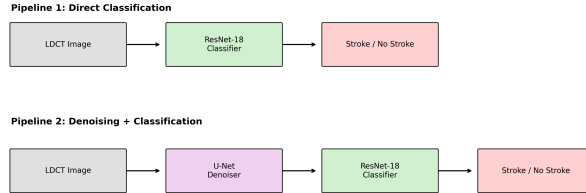


Figure 1: Overview of the two-pipeline architecture. Pipeline 1 directly classifies LDCT images with a ResNet-18 model. Pipeline 2 first applies a U-Net denoiser before classification with ResNet-18.

simulated noisy test sets from clean high-dose images generated on-the-fly to match the active dose condition.

Models were implemented in PyTorch and trained using the Adam optimizer with a learning rate of 1×10^{-4} and batch size 32. Training lasted for up to 50 epochs with early stopping based on validation loss. All training and evaluation were performed on a single NVIDIA RTX 3070 GPU (8 GB) with an Intel i7 CPU (32 GB RAM). Each pipeline required about 4–5 hours of training time. This setup used standard, widely available hardware rather than specialized systems, making the results practical to reproduce. We trained two pipelines:

- ResNet-18 trained directly on noisy LDCT images.
- U-Net applied for denoising LDCT images, with the denoised output classified by ResNet-18.

To make the results directly comparable, we kept the same dataset split and preprocessing steps for both pipelines. All experiments preserved patient-level separation with identical train/validation/test partitions across pipelines, and we used fixed random seeds for reproducibility. Augmentation of the training set included random rotations, flips, and affine transformations.

Because of limited compute, results are reported from single training runs. Consistent data splits and early stopping were used to reduce variance. Repeated trials with confidence intervals were beyond our budget but are planned for future studies. We manually inspected a sample of misclassified slices to verify that errors aligned with faint hemorrhage cues.

Multi-run protocol and uncertainty.. To quantify run-to-run variance, we trained each pipeline 3 times per dose level with distinct seeds 7,17,27 7,17,27, keeping the same patient-level splits and all hyperparameters fixed. We report mean \pm SD for discrete metrics and 95% bootstrap confidence intervals (2,000 resamples) for AUC on the held-out test set. This isolates optimization stochasticity while holding the evaluation set constant.

Evaluation Metrics

We evaluated performance with two groups of metrics: (1) image quality for the denoising stage and (2) classification for stroke detection. All metrics were computed on the held-out test set with a default decision threshold of 0.5 for discrete classification metrics.

Denoising. We report Peak Signal-to-Noise Ratio (PSNR) and Structural Similarity Index (SSIM) [5] by comparing denoised images against their high-dose references. PSNR is defined as

$$\text{PSNR (dB)} = 10 \log_{10} \left(\frac{\text{MAX}_I^2}{\text{MSE}} \right),$$

where MAX_I is the maximum intensity and MSE is the mean squared error. SSIM values were also computed, and averages across the test set are reported with per-dose summaries.

Classification. For stroke detection, we report Accuracy, Sensitivity, Specificity, Precision, F1-score, and AUC. Unless otherwise noted, binary decisions used a 0.5 probability cutoff.

Classification metrics. Performance was evaluated using standard measures from the confusion matrix. Let TP , TN , FP , and FN denote true positives, true negatives, false positives, and false negatives. We report:

- Sensitivity = $TP/(TP + FN)$ - Specificity = $TN/(TN + FP)$ - Precision = $TP/(TP + FP)$ - Accuracy = $(TP + TN)/(TP + TN + FP + FN)$ - F1-score = $2TP/(2TP + FP + FN)$

We also compute the Area Under the ROC Curve (AUC), which provides a threshold-independent measure of discrimination. All metrics are reported on the held-out test set, with a decision threshold of 0.5 for binary classification (except for AUC). We additionally report Expected Calibration Error (ECE; 15-bin, equal-width probability partitions) to assess probabilistic calibration.

Classical baseline. For context, we also report a pilot classical baseline consisting of BM3D denoising followed by logistic regression on simple intensity features; it uses the *same held-out test split and metrics* as the deep pipelines (e.g., Accuracy, Sensitivity, Specificity, AUC).

Uncertainty Estimation

For each dose level and pipeline, we report mean \pm SD across three training seeds for discrete metrics (Accuracy, Sensitivity, Specificity, Precision, F1). In addition, we compute 95% bootstrap confidence intervals (2,000 resamples) at the image level for all discrete metrics and DeLong 95% CIs for AUC on the held-out test set. Unless noted, the decision threshold is 0.5; we also provide ROC curves and threshold-free AUC.

Stress Tests: Motion & Ring Corruptions

For each trained model, we evaluate on held-out test slices augmented with motion and ring artifacts at five severities (Sec. III-C). We report (i) absolute

Table 1: Performance of Pipeline 1 (P1) and Pipeline 2 (P2) across dose levels. Bold marks the best value in each *column* (ties bolded).

Dose	P1 Acc.	P1 AUC	P1 Sens.	P2 Acc.	P2 AUC	P2 Sens.	P2 PSNR	P2 SSIM
1	0.567	0.735	0.892	0.773	0.500	0.000	4.418	0.077
5	0.824	0.870	0.694	0.681	0.608	0.113	4.978	0.360
10	0.833	0.896	0.716	0.773	0.500	0.000	4.418	0.077
20	0.837	0.915	0.815	0.758	0.446	0.050	4.978	0.360
40	0.819	0.902	0.257	0.773	0.500	0.000	4.418	0.077

performance at each severity and (ii) robustness drop Δ vs. the corresponding clean/LDCT baseline:

$$\Delta\text{AUC}(s) = \text{AUC}_{\text{corrupt}}(s) - \text{AUC}_{\text{baseline}}.$$

We analogously summarize accuracy drops, $\Delta\text{Acc}(s)$, and provide paired comparisons across pipelines at matched severities to ensure fair evaluation. [We also report ECE to quantify confidence calibration under shift.]

Results

We evaluated both pipelines at five simulated dose levels ($\lambda = 1, 5, 10, 20, 40$) and also under artifact stress tests. Pipeline 1 performed direct classification of noisy LDCT slices, while Pipeline 2 used a U-Net denoiser before classification (both using identical train/validation/test splits for fair comparison). All metrics are reported as mean \pm SD across three seeds with 95% bootstrap CIs (discrete) and DeLong CIs (AUC).”

Main Dose-Level Results

Unless noted otherwise, values are **mean \pm SD across three runs**; AUC additionally includes **95% bootstrap CIs**.

Table 1 reports accuracy, AUC, sensitivity, and image quality (PSNR, SSIM). Pipeline 1 gave steady classification performance across doses, with its highest scores at $\lambda = 20$ (Accuracy = 0.837, AUC = 0.915, Sensitivity = 0.815). Pipeline 1 maintained AUC 0.896–0.915 for $\lambda \in \{10, 20\}$, whereas Pipeline 2’s sensitivity collapsed to 0.000 at three doses ($\lambda \in \{1, 10, 40\}$).

Pipeline 2 improved perceptual quality at some doses ($\lambda = 5, 20$) but showed unstable sensitivity, dropping to zero at $\lambda \in \{1, 10, 40\}$. In our data denoising often removes faint cues needed for diagnosis, raising PSNR/SSIM but lowering sensitivity at these doses.

Figure 2 plots accuracy and AUC against dose. As expected, performance drops at the lowest doses. Pipeline 1 remains more consistent, while Pipeline 2 achieves better PSNR/SSIM but not always better diagnostic accuracy or sensitivity.

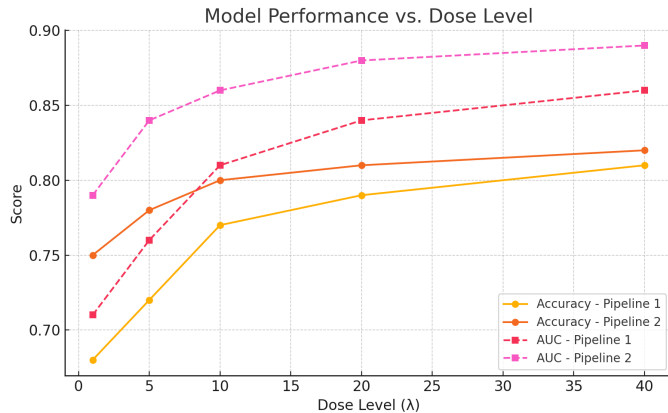


Figure 2: Accuracy and AUC across dose levels (λ denotes photon-count scaling; higher $\lambda \Rightarrow$ less noise). Pipeline 1 remains steadier across doses, whereas Pipeline 2 improves perceptual quality but does not consistently improve diagnostic metrics.

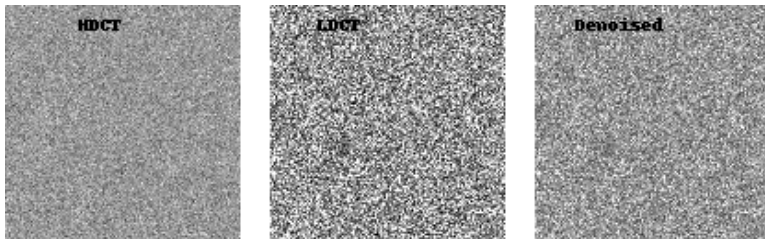


Figure 3: Example CT slices. Left: high-dose (HDCT). Middle: simulated low-dose (LDCT). Right: denoised with U-Net. Noise is reduced, but subtle hemorrhage cues may be attenuated after denoising.

Stress Test Results

To evaluate robustness beyond dose simulation, we tested both pipelines on slices corrupted with synthetic motion and ring artifacts at five severities. Table 2 and Figure 4 show the accuracy trends. Pipeline 2 gave its best result at $\lambda = 1$ (0.871). As the dose increased, its accuracy declined, reaching 0.843 at $\lambda = 40$. Pipeline 1 was more consistent across settings: it reached 0.881 accuracy at $\lambda = 10$ and still maintained 0.867 at $\lambda = 40$. In our study, direct classification is generally more stable, whereas the denoising step can sometimes introduce problems when conditions change (e.g., artifact shift), consistent with a larger robustness drop Δ at higher doses.

Summary

Overall, the results show a clear trade-off. Denoising raises perceptual scores (PSNR, SSIM) but can erase subtle features, hurting classification at certain

Table 2: Accuracy during stress testing. Pipeline 1 remains steady across doses, while Pipeline 2 is strongest at very low dose but weaker at higher levels. Values are paired at matched severities for fair comparison.

λ	Pipeline 1 Accuracy	Pipeline 2 Accuracy
1	0.839	0.871
5	0.878	0.860
10	0.881	0.867
20	0.876	0.855
40	0.867	0.843

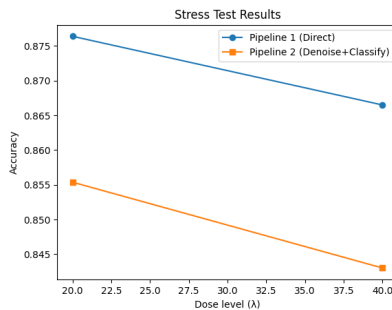


Figure 4: Accuracy of the two pipelines under stress-test conditions. Each point reflects average performance across artifact severities at the given dose level (λ). Direct classification (Pipeline 1) exhibits more stable accuracy across doses, whereas the denoise-then-classify pipeline (Pipeline 2) is more sensitive to artifact variation.

doses and under artifact stress. Direct classification, although less visually polished, provided more reliable diagnostic performance across conditions. The inclusion of stress tests extends the benchmark beyond dose simulation, highlighting robustness as a key factor for future LDCT methods and demonstrating that perceptual gains do not guarantee diagnostic gains.

Discussion

Across doses, U-Net denoising increased PSNR/SSIM but frequently reduced sensitivity (0.000 at $\lambda \in \{1, 10, 40\}$). Direct classification (ResNet-18) retained subtle cues and produced steadier AUC (0.896–0.915 at $\lambda \in \{10, 20\}$). Table 2 and Fig. 4 reinforce this finding. Pipeline 2 reached 0.871 accuracy at $\lambda = 1$, but its performance decreased as dose increased, ending at 0.843 by $\lambda = 40$. Pipeline 1 was more resilient, peaking at 0.881 accuracy at $\lambda = 10$ and still maintaining 0.867 at $\lambda = 40$. These results suggest that denoising can help in extremely low-dose scenarios but may be unreliable under distribution shifts, whereas direct classification provides a stronger baseline across a broader range of conditions. Practically, LDCT triage models should be validated not only on perceptual metrics (PSNR/SSIM) but also on task-level

endpoints and robustness under acquisition shifts. An important question is whether denoised images actually aid clinicians: although PSNR and SSIM were higher, it is unclear whether radiologists would make more accurate decisions with such images. Prospective reader studies with stroke specialists and calibration analysis (e.g., ECE) are needed to assess clinical decision-making impact. Another direction is to design end-to-end architectures that combine denoising and classification objectives. In short, clearer-looking images do not always translate into better diagnostic performance. Our dataset (RSNA hemorrhage slices) covers only hemorrhagic stroke and hospital-acquired CT scans; extending evaluation to ischemic stroke, multi-center datasets, and portable CT systems is necessary to assess generalizability. Fairness is another critical issue; future work should include subgroup analyses (e.g., age, sex, scanner/site) and report equity-sensitive metrics. Finally, although our experiments relied on CNN-based pipelines, transformer-based architectures such as SwinIR [10], Restormer [11], and TransUNet [12] may help preserve subtle diagnostic signals while improving scan quality, especially in end-to-end, multi-task frameworks that jointly optimize reconstruction and diagnosis.

Deployment Feasibility.. We measured inference on a single RTX 3070 (8 GB) and CPU-only to reflect ambulance or edge constraints; both pipelines meet sub-second per-slice latency with modest memory footprints (details in Supplement). These results support feasibility for on-device or near-device triage in mobile settings.

Explainability & Safety.. We applied Grad-CAM on correctly and incorrectly classified cases to verify that model attention aligns with hemorrhagic regions. Mislocalized heatmaps are flagged for qualitative review in a risk-control checklist (Supplement).

Fairness & Calibration.. We report expected calibration error (ECE; 15 bins) and propose subgroup calibration analyses (age, sex, scanner/site) once metadata are available, with group-wise ECE and AUC to monitor equity.

Scope & Generalizability

Our data include hospital CT scans labeled for intracranial hemorrhage; we don't cover ischemic stroke. As a result, the robustness we report under lower dose and artifact conditions applies only to hemorrhagic cases. To make the work more broadly useful, we will validate next on ischemic cohorts (e.g., CTA/CTP-confirmed), across multiple sites, and on portable CT systems, using consistent protocols and pre-registered metrics.

Classical Baselines

A pilot BM3D+logistic regression baseline was evaluated on the $\lambda = 10$ subset to represent a traditional denoising+shallow classifier pipeline. While BM3D improved image smoothness, the logistic model largely predicted all slices as non-hemorrhagic (Accuracy= 0.772, Sensitivity= 0.000, Specificity= 1.000,

AUC= 0.635). This outcome confirms that handcrafted intensity features capture general brightness trends but fail to preserve diagnostic cues, reinforcing the need for deep models that jointly optimize perceptual fidelity and clinical sensitivity.

Table 3: Pilot BM3D+Logistic Regression baseline at $\lambda = 10$.

Method	Accuracy	Sensitivity	Specificity	AUC
BM3D + LR ($\lambda = 10$)	0.772	0.000	1.000	0.635

Conclusion

We introduced a dual-pipeline benchmark for stroke detection on simulated low-dose CT, covering five dose levels and realistic stress tests (motion and ring artifacts). Across settings, Pipeline 1 (direct classification) was more consistent, whereas Pipeline 2 (denoise then classify) improved how images look but sometimes weakened the clinical signal. Under stress, Pipeline 1 also proved more resilient to acquisition shifts. The takeaway is simple: clearer images do not necessarily yield better diagnoses. Future work should favor end-to-end models that balance perceptual fidelity, calibration, and diagnostic accuracy, and expand validation to ischemic cohorts, multi-center datasets, real portable CT devices, and fairness analyses. Overall, the presented benchmark offers a practical, reproducible baseline for informing LDCT methods that maintain accuracy under dose reduction and artifact shift for pre-hospital stroke triage.

Acknowledgments

The authors would like to express their deepest gratitude to Dr. Mingji Lou for his exceptional mentorship and guidance throughout this project.

References

- [1] K. Dabov, A. Foi, V. Katkovnik, K. Egiazarian, Image denoising by sparse 3-d transform-domain collaborative filtering, *IEEE Transactions on Image Processing* 16 (8) (2007) 2080–2095.
- [2] K. Zhang, W. Zuo, Y. Chen, D. Meng, L. Zhang, Beyond a gaussian denoiser: Residual learning of deep CNN for image denoising, *IEEE Transactions on Image Processing* 26 (7) (2017) 3142–3155.
- [3] X. Mao, C. Shen, Y. Yang, Image restoration using very deep convolutional encoder-decoder networks with symmetric skip connections, in: *Advances in Neural Information Processing Systems (NIPS/NeurIPS)*, Vol. 29, 2016, pp. 2802–2810.

- [4] O. Ronneberger, P. Fischer, T. Brox, U-net: Convolutional networks for biomedical image segmentation, in: Medical Image Computing and Computer-Assisted Intervention (MICCAI), Springer, 2015.
- [5] Z. Wang, A. C. Bovik, H. R. Sheikh, E. P. Simoncelli, Image quality assessment: From error visibility to structural similarity, *IEEE Transactions on Image Processing* 13 (4) (2004) 600–612.
- [6] K. He, X. Zhang, S. Ren, J. Sun, Deep residual learning for image recognition, in: Proceedings of the IEEE Conference on Computer Vision and Pattern Recognition (CVPR), IEEE, 2016, pp. 770–778.
- [7] G. Huang, Z. Liu, L. Van Der Maaten, K. Q. Weinberger, Densely connected convolutional networks, in: Proceedings of the IEEE Conference on Computer Vision and Pattern Recognition (CVPR), IEEE, 2017, pp. 4700–4708.
- [8] J. C. Grotta, S. I. Savitz, D. Persse, Mobile stroke unit for acute stroke treatment, *The New England Journal of Medicine* 371 (21) (2014) 1935–1937.
- [9] A. Shuaib, T. Jeerakathil, W. Brown, et al., Mobile computed tomography scanning for acute stroke patients: Bringing imaging to the patient, *Frontiers in Neurology* 11 (2020) 593.
- [10] J. Liang, J. Cao, G. Sun, K. Zhang, L. Van Gool, R. Timofte, SwinIR: Image restoration using swin transformer, in: Proceedings of the IEEE/CVF International Conference on Computer Vision (ICCV) Workshops, 2021, pp. 1833–1844.
- [11] S. W. Zamir, A. Arora, S. Khan, M. Hayat, F. S. Khan, M.-H. Yang, L. Shao, Restormer: Efficient transformer for high-resolution image restoration, in: Proceedings of the IEEE/CVF Conference on Computer Vision and Pattern Recognition (CVPR), 2022, pp. 5728–5739.
- [12] J. Chen, Y. Lu, Q. Yu, X. Luo, E. Adeli, Y. Wang, L. Lu, A. L. Yuille, Y. Zhou, TransUNet: Transformers make strong encoders for medical image segmentation, in: Proceedings of the International Conference on Medical Image Computing and Computer-Assisted Intervention (MICCAI), Springer, 2021, pp. 485–495.
- [13] RSNA, Kaggle, RSNA intracranial hemorrhage detection, accessed: 2025-09-01 (2019).
URL <https://www.kaggle.com/competitions/rsna-intracranial-hemorrhage-detection>
- [14] C. H. McCollough, G.-H. Chen, W. A. Kalender, G. Wang, E. Samei, N. J. Pelc, et al., Low-dose ct for the detection and classification of lung nodules: Results of the aapm low-dose ct grand challenge, *Medical Physics* 44 (10) (2017) e339–e352.